Image-Based Model of Atrial Anatomy and Electrical Activation: A Computational Platform for Investigating Atrial Arrhythmia

Jichao Zhao*, Timothy D. Butters, Henggui Zhang, Ian J. LeGrice, Gregory B. Sands, Bruce H. Smaill

***Abstract*—Computer models provide a powerful platform for investigating mechanisms that underlie atrial rhythm disturbances. We have used novel techniques to build a structurally-detailed, image-based model of 3D atrial anatomy. A volume image of the atria from a normal sheep heart was acquired using serial surface macroscopy, then smoothed and down-sampled to 50 μm^3 resolution. Atrial surface geometry was identified and myofiber orientations were estimated throughout by eigen-analysis of the 3D image structure tensor. Sinus node, crista terminalis, pectinate muscle, Bachman's bundle and pulmonary veins were segmented on the basis of anatomic characteristics. Heterogeneous electrical properties were assigned to this structure and electrical activation was simulated on it at 100 μm^3 resolution, using both biophysically-detailed and reduced-order cell activation models with spatially-varying membrane kinetics. We confirmed that the model reproduced key features of the normal spread of atrial activation. Furthermore, we demonstrate that vulnerability to rhythm disturbance caused by structural heterogeneity in the posterior left atrium is exacerbated by spatial variation of repolarization kinetics across this region. These results provide insight into mechanisms that may sustain paroxysmal atrial fibrillation. We conclude that image-based computer models that incorporate realistic descriptions of atrial myofiber architecture and electrophysiologic properties have the potential to analyse and identify complex substrates for atrial fibrillation.**

***Index Terms*—Structure tensor analysis, myofiber organisation, posterior left atrium, atrial electrical activation, atrial fibrillation**

I. Introduction

Atrial fibrillation (AF) is the most common heart rhythm disturbance. AF leads to diminished quality of life and significantly increases the risk of stroke; it is associated with a range of cardiovascular diseases, including heart failure, and its incidence increases with age. Percutaneous catheter ablation is widely used to treat AF that is refractory to drug treatment and cardioversion [1]. Despite the success of this approach, more detailed understanding of the mechanisms responsible for initiation and maintenance of AF is required for optimal, patient-specific guidance of ablation of AF substrate.

Ectopic electrical activity in the pulmonary vein (PV) sleeves is a key trigger for paroxysmal AF [2]. It has been argued that abrupt changes in wall thickness and myofiber orientation experienced by these ectopic impulses as as they enter the posterior left atrium (PLA) may give rise to conduction delay and wavebreak [3]. Markedly different action potential duration (APD) in PV sleeves and adjacent left atrium could also contribute to the development of reentry under these circumstances [4,5]. That said, there is compelling evidence that other atrial substrates are involved in sustaining persistent AF [2]. Complex chamber anatomy, preferential conduction pathways and heterogeneous repolarization dynamics provide potential substrates for electrical re-entry across right and left atria and the probability of reentry is further amplified by the structural and electrical remodeling which occurs with long-standing AF, aging and heart disease [1,2].

Anatomically and electrophysiologically realistic computer models provide a powerful platform for analysing the mechanisms that underlie atrial re-entrant arrhythmias. This view has motivated the development of numerous models of atrial electrical function [6]-[13]. The structural complexity of the atria has made it difficult to quantify the 3D distribution of myocytes fully. Therefore, atrial electric properties in many models have been assumed to be isotropic, although some models have included prescribed local anisotropy to account for the role of specialized conduction tracts such as Bachman's bundle (BB) [8-10]. A promising alternative approach has been a rule-based approach [11] that enables descriptive information about atrial myofiber architecture acquired by systematic anatomic investigation of human hearts [14,15] to be incorporated into patient-specific volumetric models derived from 3D cardiac imaging data [12].

Recently, we have developed a novel image-based representation of atrial anatomy in the sheep heart that incorporates detailed information about myofiber organization throughout the atrial chambers [13]. We demonstrated that muscular architecture plays a crucial role in the normal spread of atrial electrical activation, particularly in the PLA, and that rapid changes in wall thickness and myofiber organisation adjacent to the PV junctions increase the risk of electrical instability. However, the role of atrial myofiber organization was probed by comparing the simulated spread of electrical activation with spatially uniform, isotropic and axially anisotropic electric properties.

Manuscript received February 15, 2012, revised August 7, 2012, and accepted November 5, 2012. This work was supported by the Health Research Council of New Zealand.

J. Zhao, I.J. LeGrice, G.B. Sands and B.H. Smaill are with Auckland Bioengineering Institute, University of Auckland, New Zealand. I.J. LeGrice and B.H. Smaill have joint position in Physiology Department. (Correspond to Dr. Zhao, Phone: 0064-9-923-6505; e-mail: j.zhao@auckland.ac.nz).

T.D. Butters and H. Zhang are with School of Physics and Astronomy, University of Manchester, Manchester, UK.

In this paper, we (i) describe the development of our image-based representation of atrial anatomy more completely than has been possible previously (ii) consider the effects of heterogeneous electrical properties on the spread of atrial activation in this model, and iii) investigate the hypothesis that structural anisotropy and spatial variation of repolarization kinetics contribute jointly to the probability of electrical instability in the PLA.

II. Methods

The atria from a normal sheep heart were studied. All procedures were approved by the Animal Ethics Committee of The University of Auckland and conforms to the *Guide for the Care and Use of Laboratory Animals* (NIH publication No. 85-23).

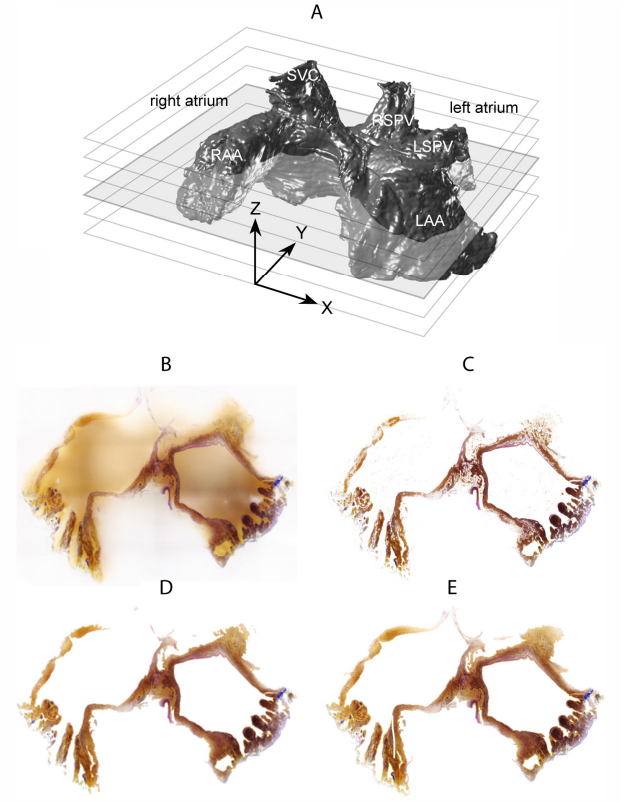

Fig. 1. (**A**) Volume image of the sheep atria acquired by serial surface imaging. Anterior view of 3D reconstruction of epicardial surface. The superior vena cava (SVC), right superior pulmonary vein (RSPV), left superior pulmonary vein (LSPV), right atrial appendage (RAA) and left atrial appendage (LAA) are indicated. (**B-E**) Processing and segmentation of the atria images. (**B**) Typical composite 2D image section prior to processing. (**C**) after application of Hessian filter and region growing correction. (**C**) after dilation and erosion process to close boundaries. (**D**) Section at same location as **A** after 3D interpolation and smoothing.

A. Image Acquisition

A crossbred sheep (45 Kg) was anaesthetized and cardiac arrest was induced *in situ* by rapid intracoronary infusion of potassium citrate. Heart and lungs were excised, immersed in cooled (4°C) physiological saline and the coronary circulation was perfused with cardioplegic solution. The PVs were ligated >1 cm from the veno-atrial junction and the lungs were removed. The ventricles were transected, mitral and tricuspid valve leaflets were removed and the atria were immersed in physiological saline, with the roof lowermost. The atria were slowly filled with warm (50°C) 6% gelatine to prevent their collapse during subsequent fixation. Once the gelatine had set, formalin (3% in phosphate buffer) was perfused through the coronary circulation for 30 minutes and the atria were immersed in this fixative for a further 12 hours. They were then placed in a plastic cylinder, stabilized with additional gelatine and imaged in a 4.7T MR scanner (Varian Inc., Palo Alto, CA). Subsequently, the atria were extracted from the gelatine, supported in an open stainless steel frame and dehydrated in a graded ethanol series. Finally, they were embedded in paraffin wax (Kendal Paraplast, 56°C melting point) using an automatic processor (TISSUE-TEK VIP 2000, Sakura, Torrance, CA).

Extended-volume surface imaging [16] was used to reconstruct 3D tissue architecture. The upper surface of the embedded atria was planed with a variable speed ultramiller (Leica SP2600, Leica Microsystems AG, Wetzlar, Germany), etched with 25% xylol in 100% ethanol and stained to a depth of ~2 µm with Toluidine blue (0.12% in 1% borax). Four overlapping images of the surface were acquired at 8.33 µm pixel resolution using a digital camera fitted with a 65 mm macro lens (Canon 1D MkII and Macro Photo MPE, Canon, Tokyo, Japan). Cross-correlation was employed to register atrial tissue structure in the four images and a composite surface image was constructed. This process was repeated at 50 µm steps throughout the volume. A schematic of the image acquisition process is given in Fig 1A.

B. Image Processing

A multi-scale structure filter, initially developed by Frangi and co-workers [17], was used to enhance contrast between myofibers and extracellular space in the composite image sections. The Hessian matrix H_r was constructed as follows:

$$H_r = \begin{pmatrix} I^r{}_{x^2} & I^r{}_{xy} & I^r{}_{xz} \\ I^r{}_{xy} & I^r{}_{y^2} & I^r{}_{yz} \\ I^r{}_{xz} & I^r{}_{yz} & I^r{}_{z^2} \end{pmatrix}, \quad \text{where} \quad I^r = K_r * I \qquad 1)$$

I is the 8-bit color intensity at each voxel in the 3D volume image and I^r is formed by convolution with an isotropic Gaussian filter K_r where r is the standard deviation. $I^r{}_{ij}$ are the second derivatives of I^r at each voxel with respect to the Cartesian image coordinates (x,y,z). Filtering was applied with a predetermined set of standard deviation values r, selected to identify atrial muscle bundles across a range of spatial scales. Application of the Hessian filter (i) reduced noise (ii) removed background color inside the atria and adjacent to their epicardial surfaces, and (iii) minimized yellow coloration of the extracellular space surrounding myocytes and muscle bundles caused by wax infiltration (see Fig 1C). Artifactual suppression by the Hessian filter of tissue areas with low stain

intensity was corrected using a region growing method. Internal structures were then connected and atrial surface boundaries closed by applying sequential dilation and erosion operations (see Fig. 1D).

These procedures were applied to each of the individual sections in the image stack. The 2D sections were then down-sampled to produce an image volume with isotropic 50 μm^3 voxels and a sequence of 3D image processing steps was applied to this volume. These included i) 3D interpolation and smoothing ii) sequential 3D erosion and dilation operations to fill small holes in epicardial or endocardial surfaces and remove "islands" not connected to them, and iii) removal of residual unconnected regions. The segmented atrial section from the processed 3D image volume that best matches the raw 2D section in Fig. 1B is presented in Fig. 1E.

C. Extracting Myofibre Orientations from the Image Structure Tensor

Local axes that represent principal structural directions were estimated throughout the image volume from the structure tensor [18]. This approach generalizes gradient intensity based methods that have been employed widely to extract the orientation of structures in 2D images [19,20] to 3D. The structure tensor for any voxel, is given by:

$$\mathbf{J} = \begin{bmatrix} I_x I_x & I_x I_y & I_x I_z \\ I_y I_x & I_y I_y & I_y I_z \\ I_z I_x & I_z I_y & I_z I_z \end{bmatrix} \qquad 2)$$

where I_x ,I_y and I_z are estimates of intensity gradient for that voxel with respect to the imaging coordinate system (x,y,z). The eigenvectors of this symmetric tensor characterize local principal structural directions [18].

The structure tensor was constructed from the image volume, smoothed with a Gaussian kernel and eigen-analysis was used to extract 3D gradient information [21]. A problem with 3D intensity gradient-based techniques is that they amplify the effects of misalignment and intensity variation between serial images. To minimize artifacts arising from this, the image volume was smoothed with an anisotropic diffusion filter guided by 3D image gradients [22] before constructing the structure tensor. This reinforced principal structural directions, but suppressed image gradients associated with intensity variation between successive image planes.

The structure tensor detects the abrupt changes in contrast at boundaries between myocytes and the non-strained space that surrounds them in our 3D atrial image volume. The spatial resolution of the downsampled image is 50 um^3, just sufficient to register individual cells and the strongest image gradients are generated by bundles of myocytes in the plane transverse to the myofiber direction. Eigen-analysis of the structure tensor therefore allowed us to identify myofiber orientation at each voxel (given by the eigenvector paired with the smallest eigenvalue). Finally the 3D fiber field was smoothed by averaging at each voxel across a 3×3×3 voxel domain. To do this, all angles were converted to corresponding points on the unit circle [23]. That is,

$$\tilde{\theta} = \tan^{-1} \frac{\sum_1^N \sin\theta_i}{\sum_1^N \cos\theta_i}, \text{ N = 27} \qquad 3)$$

The robustness of this approach was confirmed by systematic comparison of local myofiber orientation estimates with corresponding regions in the raw serial images. Because in-plane pixel dimensions in these sections are 8.33 µm, it was possible to identify the projections of individual myocytes and visually check the validity of estimated myofiber orientation.

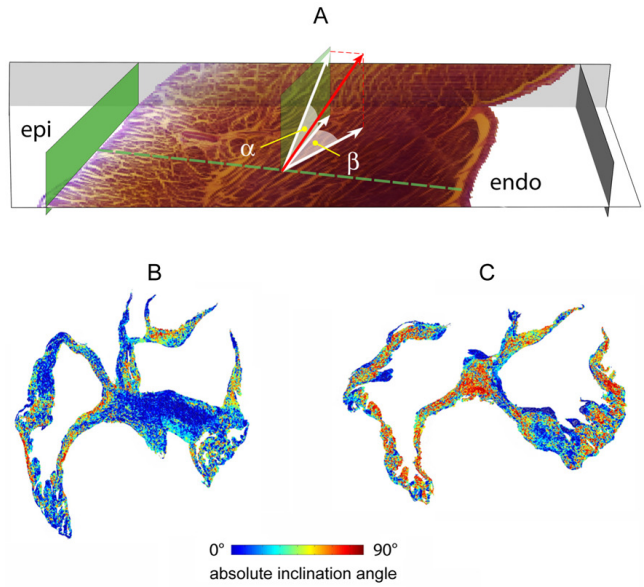

Fig. 2. Atrial myofiber orientation (**A**) Inclination angle α and transverse angle β of local atrial myofiber vector. The red arrow indicates myofiber orientation at a point in a horizontal X-Y plane. The inclination angle α is the projection of this vector onto a vertical plane parallel to the epicardial boundary. This angle is measured with respect to the horizontal and has values in the range -90° to 90°. The transverse angle β is the projection of the fiber vector onto the horizontal plane, with respect to the surface tangent plane defined above. **(B)** and **(C)** Myofiber inclination in representative sections at Z = 17.5 mm and 12.5 mm, respectively, where distances were measured from the bottom of stack. Spectrum represents absolute myofiber inclination angle with respect to X-Y plane.

Atrial myofiber orientation was specified by defining the inclination angle α and the transverse angle β of the fiber axis (see Fig 2A). The former is the projection of the fiber vector onto a vertical plane parallel to epicardial or endocardial surfaces and is measured with respect to the horizontal. The latter is the projection of the fiber vector onto the horizontal plane and is measured with respect to the surface tangent plane.

D. Regional Segmentation of 3D Atrial Anatomy

Specific atrial regions were segmented from the reconstructed atrial image volume using well-established anatomic criteria. Like others in this field [14,15], we have identified crista terminalis (CT), BB and pectinate muscles (PMs) on the basis of morphology, location and ordered myofiber architecture. The endocardial profile of the CT was

visible in serial images acquired between the veno-atrial junctions of superior and inferior vena cavae (SVC and IVC, respectively) and from this we estimated the centre of the CT in each image section. A 3D line was then fitted to these data. Because the intramural extent of the CT was less distinct than the endocardial boundary, tissue within a 5 mm radius of the 3D center line was defined as CT. Segmentation of the sinus node (SN) was somewhat more arbitrary; it was identified in X-Y image planes as a transmural region bounded by the CT and the junction of SVC and right atrial appendage (RAA) (see Fig 3C).

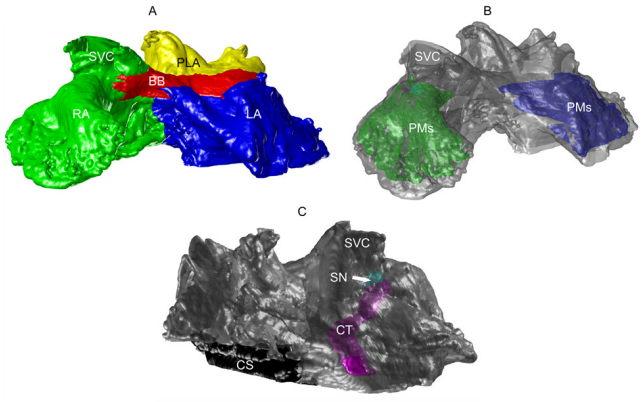

Fig. 3. Atrial Subdivision of atria into different regions. **(A)** and **(B)** Anterior views of 3D epicardial surface indicating the segmentation of right atrium (RA) - green, left atrium (LA) - blue, Bachman's bundle (BB) - red, posterior left atrium (PLA) -yellow, and right and left pectinate muscles (PMs) - green and blue, respectively. **(C)** Posterior view of 3D epicardial surface indicating locations of sinus node (SN) - light blue, crista terminalis (CT) - cyan, and coronary sinus (CS) - black.

The right and left atria (RA and LA, respectively) were separated along the inter-atrial groove. Consistent with others [3], we define the PLA (Figures 3A) as that region of the LA bounded by the inter-atrial septum, by the BB and circumferential fibers continuous with it along its anterior margin and by the mitral groove along its posterior margin. The PLA is also shown in Figures 5B and 7A, and contains the PV junctions, the LA roof and the posterior wall of the LA.

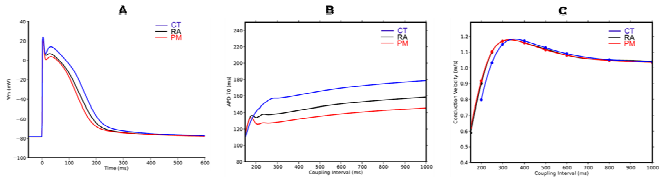

Fig. 4. Action potential morphology and restitution properties at representative atrial sites with modified Courtemanche, Ramirez and Nattel (CRN) cell activation models. **(A)** Action potentials in right atrium (RA), Pectinate muscles (PM) and Crista Terminalis (CT) at a coupling interval (CI) of 1000 ms **(B)** Action potential duration at 70% of repolarization (APD70) and **(C)** Conduction velocity (CV) as functions of CI at the same sites.

E. Modeling Atrial Electrical Activity

The spread of electrical activation in myocardial tissue can be simulated by solving the monodomain equation

$$\nabla \bullet (\sigma_i \nabla V_m) = A_m \left(C_m \frac{\partial V_m}{\partial t} + I_{ion} \right) \qquad 4)$$

where the tensor σ_i represents the tissue conductivity, V_m is the transmembrane voltage, while A_m and C_m are membrane cross-sectional area and membrane capacitance. I_{ion} is the net current carried by transmembrane ion channels.

Electrical heterogeneity was introduced into this model employing an approach outlined previously by Seemann [8] and Aslanidi [10] and colleagues. These workers modified the human atrial cell model developed by Courtemanche, Ramirez and Nattel [24] on the basis of voltage-clamp recordings from different regions in the dog atria (subsequently referred to as the CRN model). They rescaled key transmembrane currents to best match experimental data, and, where intracellular potential recordings only were available, currents were inferred from measured action potential (AP) morphology. We have further scaled these cell models so that the overall regional variation in AP morphology is preserved, but the APD range matches most closely that observed experimentally in the sheep [25]. For the RA cell model, we altered the following ionic currents: I_{Na} was reduced by 50%, I_{to} and I_{Kur} by 70%, and I_{Ca} by 20%. Additionally, the reversal potential of I_{K1} was shifted -5 mV, and the activation time-constant was reduced by 10%. The scaling factors previously applied to the CRN model to create regionally varying activation models for the human atria [8,10] were also applied in the sheep. APs simulated for different atrial regions are presented in Fig 4A, while CV and APD restitution relations for these regions are given in Figs 4B and 4C, respectively.

The three current Fenton-Karma [26] cell model was used for computationally demanding simulations (for instance, repeated cycles of activation in studies of reentry). The kinetics of the Fenton-Karma model were adapted to closely match action potential shapes and APD restitution relationships observed experimentally or simulated with our modified CRN model using methods outlined in detail elsewhere [27,28].

Axially anisotropic electrical properties were assigned to connected atrial myocyte bundles and regions characterized by ordered myofiber organization. For PMs, CT and BB, conductivities in myofiber direction (σ_f) and transverse to this (σ_t) were set to 11.7 mS and 0.9 mS, respectively. In the PLA, σ_f and σ_t were set to 9 mS and 0.9 mS, while remaining atrial regions were assumed to be uniformly isotropic. These electrical properties give rise to conduction velocities (CVs) ~1.3 m/s and ~0.6 m/s in fiber and cross-fiber directions in CT, BB and PMs, and ~1.15 m/s and ~0.65 m/s in these directions in the PLA. CV in the rest of the atria is ~ 0.75 m/s in all directions. These results are consistent with experimental estimates of regional CV in dog [29-33], sheep [3,25,34] and man [35]. CVs between 0.7 and 1.3 m/s have been reported for

the CT [29,30], but optical mapping studies in the sheep [34] suggest maximum velocities greater than this. Measured CVs for BB range from 0.92–1.67 m/s [31,32] and for the PMs from 1.0–1.54 m/s [32,33]. We estimate velocities > 1 m/s between right and left PVs from reported data in the sheep PLA [3] with much slower propagation transverse to this. Finally, CV estimates for working atrial myocardium range from 0.32 to 1.03 m/s [25,35].

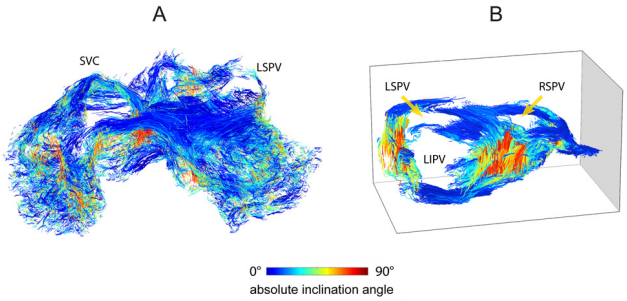

Fig. 5. Myofiber architecture in atria. **(A)** Myofiber tracks rendered on antero-superior view of atria. **(B)** 3D fiber tracks rendered on posterior view of posterior left atrium. Left superior pulmonary vein (LSPV), left inferior pulmonary vein (LIPV) and right superior pulmonary vein (RIPV) are indicated. Spectrum represents absolute myofiber inclination angle with respect to X-Y plane.

F. Numerical and Computational Methods

Our model of 3D atrial anatomy consists of 2.48×10^8 spatial points at full resolution (50 μm^3 voxels). Atrial electrical activation was simulated by solving the monodomain version of the reaction-diffusion equation (4) on a voxel-based finite difference grid derived from this volume. Solutions were obtained at 100×100×100 μm^3 for the complete atria and at 50×50×50 μm^3 resolution for the PLA with a time step of 0.0025 ms. Simulations with the modified CRN cell model were performed using either MPI or openMP using an 8 core Intel Xeon 2.67 GHz machine with 48 GB of RAM at the University of Manchester. Simulations using the Fenton-Karma activation model were parallelized under openMP and run on an IBM3850 (32 dual thread Intel chips, 256 GB shared memory, Linux operating system) at the University of Auckland. In the latter case, 1 s of activation could be simulated for the complete atria in around 30 hours.

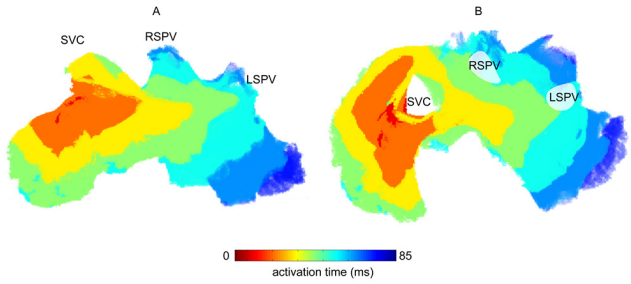

Fig. 6. Epicardial spread of electrical activation simulated on 3D atrial model incorporating myofiber orientation data and heterogeneous electrical properties. Activation isochrones are rendered on antero-superior and superior views of the atria in **(A)** and **(B)**, respectively. Activation time key for the color map (indicated) same for both.

III. RESULTS

A. Image-Based Model of 3D Atrial Anatomy

Atrial myofiber arrangement throughout the atria was visualized using 3D fiber tracking techniques [36]. In Fig 5, fiber tracts are viewed from the epicardial surface, which masks intramural structures. Despite this, key anatomic features are evident. In Fig 5A (an anterior view of RA and LA), these include (i) BB, which originates in the RA near the origin of the SVC and runs across the anterior roof of the LA, and (ii) longitudinal myofibers immediately below BB in the groove between the RA and LA. The intramural extent of BB and the bundles in the inter-atrial septum are clear in Figures 2B and 2C, respectively.

Also evident in these figures, is the lack of uniform regional variation in myofiber orientation in the atria. There are large changes in the orientation of some adjacent myocyte bundles and in some regions no net direction is evident. This organization was confirmed by inspection of the high-resolution image sections from which the volume is derived.

Figure 5B, presents a magnified view of the PLA. The cellular architecture of the PLA is complex, but surprisingly ordered. Myofibers wrap circumferentially around all four PVs adjacent to the veno-atrial junctions and also run from anterior to posterior margins of the PLA between right and left PVs. There are abrupt changes in geometry and myofiber orientation at the junction of the PVs with the LA. The PV sleeves are thin-walled, but wall thickness increases markedly as the veno-atrial junction is approached. Also, myofibers are predominantly aligned with the cylindrical axis in some epicardial regions of the PV sleeves and these suddenly rotate through ~90° at the veno-atrial junction.

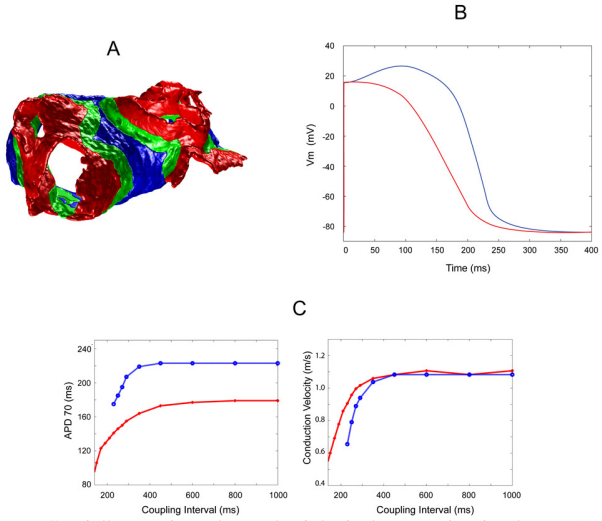

Fig. 7. Spatially varying electrophysiological properties in the PLA. **(A)** Segmentation of PLA. PV sleeves and veno-atrial junctions are indicated in red and LA tissue in blue. The transitional region between them is shown in green. **(B)** Typical APs with adapted Fenton Karma activation model for PV sleeve and LA tissue (red and blue, respectively). **(C)** CV and APD restitution properties for PV sleeve and LA tissue (red and blue, respectively).

B. Spread of Electrical Activation in the Atria

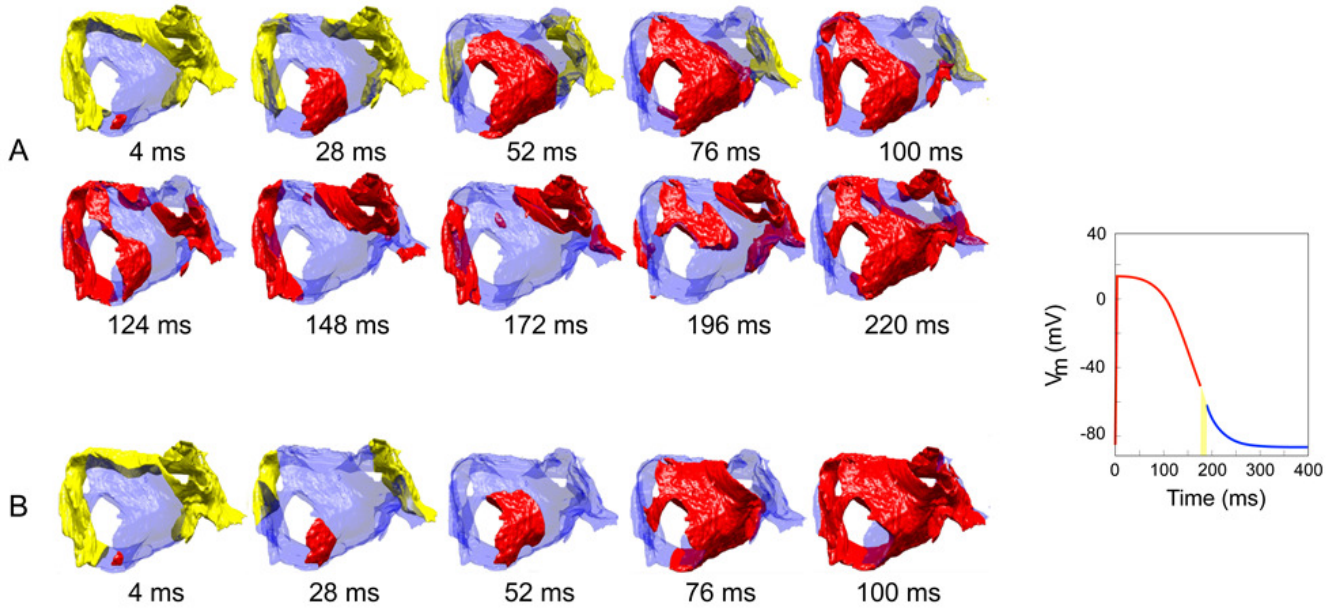

Fig. 8. Magnetization as a Effects of structural anisotropy and spatially varying electrophysiological properties on electrical stability in the PLA. Electrical activity in PLA with **(A)** anisotropic, spatially varying electrical properties, and **(B)** isotropic, uniform electrical properties. Stimulus drive train with progressively decreasing CIs applied at posterior LIPV sleeve. Cycles immediately prior to re-entry and conduction block are shown in A and B, respectively. The key to the colour maps is shown in the inset figure. Red indicates activated regions that are absolutely refractory and yellow shows regions that have entered the relative refractory period. Comparable simulations were also carried out for i) uniform anisotropic electrical properties, and ii) isotropic, spatially varying electrical properties. The results are not shown here, but are summarised in section C of the Results.

Fig. 6 shows the epicardial spread of electrical activation simulated on the image-based model of atrial anatomy from a stimulus site near the SN, assuming regionally heterogeneous electrical properties. Distinct propagation pathways are evident in the rapid spread from the SN across the superior RA into the RAA (within 35 ms) and from the RA to LA (much of the superior LA is activated within 30-45 ms). Preferential axial conduction via BB and within the PLA gives rise to early activation of the antero-superior margin of the LA and nonuniform spread across the LA roof and posterior wall between the right and left PVs. This results in substantial activation time dispersion in the vicinity of the PV junctions and, in particular, adjacent to the left inferior pulmonary vein (LIPV). Atrial activation was completed in 85 ms. Minimal difference could be discerned between the spread of atrial activation simulated with the modified CRN activation models and simpler Fenton-Karma activation models (mean voxel-by-voxel activation time difference 0.053 $\pm$ 0.224 ms).

C. Electrical Stability in the Posterior Left Atrium

We hypothesize that the structural complexity of the PLA and the marked electrophysiological differences between PLA tissue and the PVs both contribute to increased risk of reentrant electrical activity in this region. To dissect the possible roles of these two factors, we have simulated the effects of ectopic activation in the PV sleeves, using an image-based model of the PLA only. The PLA was segmented further, as shown in Fig. 7A. Regions containing left and right PV sleeves and veno-atrial junctions were defined and are shown in red. The remainder of the PLA, which is characterized by ordered myofiber organization with muscle bundles running between right and left PVs, is indicated in blue and green. Fenton-Karma cell models [26] were adapted [27,28] to reproduce CV and APD restitution properties observed experimentally in isolated canine myocytes from PV sleeves and LA [4]. These cell models were used in the PV sleeves veno-atrial junctions (red in Figure 7A) and in the region of the PLA indicated in blue in Figure 7A). Typical APs in these regions are shown in Figures 7B, while CV and APD restitution relations are presented in 7C. These data illustrate an ~80% difference in APD_{70} (APD to 70% of repolarization) between PV sleeves and the PLA between right and left PVs. There is a smooth transition in electrophysiological properties across the region shown in green in Figure 7A.

Repetitive stimulation with reducing coupling interval (CI) was imposed at the LIPV sleeve. The drive train was started at 1000 ms and CI was reduced progressively by 20 ms until conduction failure or re-entry occurred. This process was repeated for four different cases 1) anisotropic, spatially varying electrical properties 2) anisotropic, uniform electrical properties 3) isotropic, spatially varying electrical properties, and 4) isotropic, uniform electrical properties.

The results for cases 1 and 4 are presented in Figure 8; constraints on space prevent us from showing all four data sets. Conduction slowing was observed with reducing CI in all four cases studied. Marked delays and regional block were seen with anisotropic, spatially varying electrical properties, and the onset of wavebreak is evident in Figure 8A. Here, activation propagates initially around the left PVs and spreads more slowly rightward across the PLA to activate the right PVs. Wavebreak occurs ~150 ms after stimulation and is sustained by reentrant activity around the PV sleeves and

veno-atrial junctions. In contrast, with isotropic uniform electrical properties, conduction failure only was seen and at at a much lower CI (~130 ms). In Figure 8B, activation spreads in a uniform fashion from the stimulus site at the LIPV sleeve during the cycle immediately prior to conduction failure. Instability was also observed in cases 2) and 3), but at significantly lower CIs than for 1).

IV. Discussion

A. *Image-Based Model of 3D Atrial Anatomy*

Much of the current understanding of atrial myofiber arrangement is based on careful anatomic studies by Ho, Anderson and co-workers [14,15], who used dissection and macrophotography to trace fiber tracts and define preferential conduction pathways in the human atria. The anatomic findings outlined in this paper have been presented previously in greater detail [13]. The intramural fiber orientations reported by our group for the sheep atria match the picture of muscular architecture built up by systematic observation of human atria. The ordered arrangement of myocytes in CT, BB, and PMs are faithfully reproduced, as is the complex myofiber architecture of the inter-atrial septum and the LA adjacent to it. Our representation of myofiber organisation between and around the PVs is consistent with the BB, as well as the septopulmonary and septoatrial bundles described by Wang and others [14].

We find no evidence for the existence of a discrete isolating layer in the sheep septum [11], either in the series of high-resolution image sections acquired throughout the atria or after structure tensor analysis has been applied to this image volume. We do observe uniformly vertical myofiber orientation (with respect to the AV valve plane) throughout much of the atrial septum, again consistent with reports for the human atria [14].

Myofiber architecture in the PV sleeves has been characterised in greatest detail in the dog [37]. Verheule and co-workers report predominantly circumferential myofiber orientation at the veno-atrial junctions with abrupt changes in orientation in epicardial regions of the PV sleeves adjacent to this. The morphology of the human PV is thought to be similar to this [2] and post-mortem analysis of PV sleeves indicates that discontinuity in myofiber organisation is greater for patients with AF [38]. We also observe predominantly circumferential myofiber organization at the veno-atrial junctions with abrupt local changes in fiber orientation in some regions in the PV sleeves as the junctions are approached (see representation of 3D myofiber tracts in LIPV in Figure 5B).

These findings confirm that the principal features of atrial myoarchitecture are conserved in large mammalian hearts despite differences within and between species. However, the most important difference between this and earlier anatomic studies is that we have generated comprehensive, quantitative data on atrial myofiber architecture that has not previously been available.

A further novel aspect of this work is the use of the 3D structure tensor to estimate atrial myofiber orientation. Diffusion-tensor magnetic resonance imaging (DTMRI) has been used to quantify myofiber architecture in the ventricles [19], but lacks the spatial resolution to capture atrial myofiber architecture fully. Structure tensor analysis has features in common with DTMRI and it has been successfully used to characterize fiber orientations in composite materials [21]. In the present setting, the 3D intensity gradients from which myofiber orientation is determined are due to contrast variation between myocyte bundles and the extracellular space surrounding them. It should be possible to use this approach with high-resolution CT and MRI [39, 40], provided the image contrast associated with these features can be enhanced. The 50 μm^3 voxel dimensions used in this study are likely close to the limit at which the method is effective. In practise, we benefited from the 8.33 µm pixel dimensions in the initial image sections. This enabled us to visualize individual cells in these sections and check the validity of estimated myofiber orientations. However, in future we will seek to acquire image sections at 25 µm intervals and work with down-sampled image volumes with 25 μm^3 voxel dimensions.

B. *Spread of Electrical Activation in the Atria*

The activation spread predicted here in this image-based model of atrial anatomy corresponds very closely to atrial activation patterns mapped in human [41], dog [33,42] and sheep [3] in sinus rhythm or during electrical stimulation adjacent to the SN. The model replicates normal propagation through the anterior and posterior LA walls during sinus rhythm or stimulation adjacent to the SN with final activation adjacent to the LIPV, as observed in man [41] and dog [33,42]. Of particular interest is the close correspondence between simulated activation of the PLA and experimental data for the sheep reported by Klos and co-workers [3]. Our model matches the spread of electrical activation across the PLA reported by these researchers for activation from the SN and replicates the observed activation time dispersion adjacent to the left PVs. In the model, maximum and minimum CVs in the PLA were ~1.15 m/s and 0.65 m/s, again consistent with results presented by Klos et al. [3].

Although our model does not include an isolating septal layer, initial breakthrough to the LA occurs via BB with stimulation adjacent to the SN. This is a result of the axially anisotropic electrical properties that have been used. Because myofiber orientation is uniformly vertical throughout much of the septum, conduction transverse to this is inherently slow. Therefore fiber tracts which traverse the septum approximately parallel to the AV valve plane provide preferential inter-atrial conduction pathways. BB is the most prominent of these and in the model has higher CV than surrounding atrial myocardium. However there are other myofiber tracts that cross the septum and could potentially provide pathways for preferential conduction.

The assignment here of regionally heterogeneous electrical properties results in atrial activation spread that is qualitatively similar (though quantitatively different) to previous

simulations on this anatomic structure [13] in which axially anisotropic, but spatially uniform, electrical properties were assumed. The difference in the total activation times predicted in the two cases (~85 ms vs 98 ms) reflects the modestly increased axial conductivity assigned to CT, BB and PMs in this study. Electrical mapping studies indicate total atrial activation times in sinus rhythm of ~70 ms in dogs [30, 33] and ~ 105 ms in man [41]. On the basis of experimental studies [3] and dimension, we would expect times for sheep closer to dog than man. P wave duration for sheep in sinus rhythm has been reported as 66 $\pm$ 12 ms [43]. While this measure may underestimate total atrial activation time, our prediction of 85 ms is at the upper end of the expected range for the sheep. Activation spread is dominated by the magnitudes and anisotropy of the conductivities selected and some of the regional electrical properties assigned in this study require further consideration. For instance, we may have overstated the anisotropy ratio for atrial working myocardium and understated the CV for some specialized fiber tracts; we note that Krueger et al. [11] assigned anisotropy ratios of 3.75 to working myocardium and ~23 to PMs. This reinforces the fact there is uncertainty about the tissue conductivities that apply in different atrial regions and the extent to which regional electrical properties transfer across species. Systematic acquisition of high resolution maps of 3D electrical activity throughout the atria in different species is necessary to resolve these issues.

Finally, that near identical results are obtained when adapted CRN and Fenton-Karma activation models are used to simulate activation on the same representation of atrial anatomy with the same electrical properties is hardly surprising, because both incorporate very similar representations of the fast inward current. The effects of spatially varying repolarization kinetics only affect propagation at high stimulus rates, as described in the next section.

C. Electrical Stability in the Posterior Left Atrium

There is compelling empirical evidence that the muscular architecture and electrical properties of the PLA and PVs play an important role in the initiation and maintenance of AF and paroxysmal AF in particular [2]. For ectopic stimuli originating in the PV sleeves, abrupt changes in myofiber orientation and wall thickness at the junctions of the PVs and LA are thought to give rise to conduction delays, regional block and reentry [3,37]. In a previous study [13], we demonstrated that the complex myofiber pathways adjacent to BB, and around and between the PVs, could give rise to marked repolarization time dispersion that contributes further to electrical instability in this region. Although these numeric experiments were conducted on the same image-based model of atrial anatomy, cell activation behaviour was assumed to be spatially uniform in these numeric experiments, despite the considerable differences in APs recorded from PV and LA myocytes [4].

Here we have tested the hypothesis that spatial variation of repolarization kinetics contributes to electrical instability in the PLA. In doing so, we have effectively repeated the modeling study carried out by Cherry et al. [5] with a much more realistic representation of atrial anatomy. The results presented in this paper suggest that both structural anisotropy and nonuniform electrical behaviour independently contribute to the probability of electrical instability in the PLA and together markedly increase risk.

These findings contain some potentially important insights into the mechanisms that underlie paroxysmal AF. They suggest that ectopic activation originating in the PV sleeves can trigger unstable electrical activity in the PLA that is sustained by reentrant activation around the veno-atrial junctions. The unstable behaviour in Figure 8A is facilitated by structural anisotropy. Activation spreads preferentially around the PVs, because myofibers at the veno-atrial junctions are circumferentially organized and more slowly across the PLA between left and right PVs, because it is transverse to the axial direction of the myocyte bundles in this region. Spatial variation in repolarization kinetics exacerbates this activity - allowing activation in the PV sleeves and junction, but preventing coordinated activation in the central PLA. For more rigorous identification of the relative roles of structure and electrical heterogeneity in this context, it will require more detailed information on the regional variation of AP characteristics and cellular electrophysiology across the PLA and activation models that reproduce this behaviour faithfully.

D. Study Limitations and Future Work

Numerical studies of the kind described here on the structurally normal atria provide insight into factors that may contribute to paroxysmal AF. However, the mechanisms responsible for persistent AF (PtAF) are poorly understood and treatment outcomes are disappointing [1]. Ageing, heart disease and repeated episodes of AF are associated with a plethora of physical changes in the atria that heighten the risk of PtAF [2]. Experimental sheep models are increasingly being used to study PtAF [44] and if structure-based computer models are to be used to interpret these data, it will be necessary to acquire representative volumetric models of sheep atria from such animals. A problem with simulating atrial electrical activation in the sheep heart is that the electrophysiological properties of myocytes from different atrial regions have been less systematically characterized in this species than the dog [4] or the rabbit [9]. A further difficulty is that regional electrical properties, such as conductivities and anisotropy ratios, are based on limited experimental data that exhibit relatively wide variability. These issues drive much of the ongoing work in our laboratory.

Our computational approach could also be refined in a number of ways. For instance, an optimized finite mesh could provide a more efficient representation of atrial surface geometry and more systematic handling of boundary value conditions of than our current finite-difference grid. Preliminary attempts to fit finite element models to the atria are well advanced.

Simulating electrical activation on an anatomically-detailed representation of the atria with a biophysically-based cell electrophysiology model is computationally demanding, even for a single activation cycle, and numeric investigations of arrhythmia typically require long stimulus drive trains. This motivated our decision to use a lower-order activation model to investigate electrical stability in the PLA. Jacquemet [45] has recently proposed the Eikonal-Diffusion (ED) model as a means of accelerating analysis and simulation of AF. Although this approach does not provide explicit solutions of membrane potential, it enables efficient estimation of 3D atrial activation and provides initial conditions that can be used to simulate reentry with high order biophysically-based activation models. Sermesant, Ayache and coworkers have demonstrated that it is also possible to estimate regional repolarization in this context using a time-stepping method [46] or by combining the ED approach with robust low-order activation models [47].

In our study, we have opted to use the three-current Fenton-Karma cell model [26] to investigate mechanisms of reentry in the PLA, because its kinetics can be adapted to match the restitution relationships observed in the atria with acceptable accuracy [27,28]. It is noteworthy that although the biophysically-detailed CRN model replicates features of atrial AP morphology better than the Fenton-Karma model (compare Figs 4A and 7B), the latter provides a more reliable representation of observed atrial APD and CV restitution relations [25,27,28] (compare Figs 4B&C with Figs 7C). It has been demonstrated previously that the use of appropriate low-order activation models provides an effective initial means of investigating the effects of myofiber architecture and electrical heterogeneity on atrial electrical function [20]. That said, more complex biophysically-based models that incorporate realistic descriptions of calcium homeostasis will also be necessary to understand how the cellular electrical remodeling that occurs with ageing and heart disease contribute to risk of AF. Furthermore, the progressive improvement in the power of high-performance computer systems, means the use of such complex activation models is becoming increasingly practicable.

Used in conjunction with appropriate structural and experimental studies, computer models that incorporate detailed and accurate representations of atrial architecture and electrophysiology will almost certainly play a crucial role in understanding the factors that give rise to PtAF. Furthermore, such models could also provide a means of assessing the spatial scale of structural and functional information required for effective use of patient-specific computer modelling [11,12] in optimizing electrophysiological ablation outcomes. We see the current model as a step toward these ends.

V. Conclusion

In this paper, we have outlined a suite of image processing tools that have been used to construct a high-resolution image-based model of 3D atrial anatomy, which incorporates realistic surface geometry and myofiber architecture. While these techniques have been applied to serial surface imaging data, they can be readily generalized to other volume imaging modalities. We have demonstrated that accurate representations of specialized tracts such as the CT, PMs and BB and the myofiber architecture of the PLA are necessary to model the normal spread of atrial activation. Furthermore, our numerical investigation of mechanisms through which ectopic stimuli originating from the PV sleeves contribute to electrical instability in the PLA shows that structurally-detailed image-based computer models provide a powerful platform for investigating arrhythmic substrates in the atria.

Acknowledgment

We thank Dr Rita Yassi for her perseverance and skill in acquiring the atrial serial images and Dane Gerneke for his expert technical support.

References

[1] A.G. Brooks, M.K. Stiles, J. Laborderie, D.H. Lau, P. Kuklik, N.J. Shipp, L. Hsu, P. Sanders. "Outcomes of long-standing persistent atrial fibrillation ablation: a systematic review." *Heart Rhythm*, vol. 7, pp. 835-846, 2010.

[2] U. Schotten, S. Verheule, P. Kirchhof, A. Goette. "Pathophysiological mechanisms of atrial fibrillation: A translational appraisal." *Physiological Reviews,.* vol. 91, pp. 265-325, 2011.

[3] M. Klos, D. Calvo, M. Yamazaki, S. Zlochiver, S. Mironov, J-A. Cabrera, D. Sanchez-Quintana, J. Jalife, O. Berenfeld, J. Kalifa. "Atrial septopulmonary bundle of the posterior left atrium provides a substrate for atrial fibrillation initiation in a model of vagally mediated pulmonary vein tachycardia of the structurally normal heart." *Circulation: Arrhythmia and Electrophysiology,* vol 1, pp. 175-183, 2008.

[4] J.R. Ehrlich, T-J Cha, L. Zhang, D. Chartier, P. Melnyk, S.H. Hohnloser, S. Nattel. "Cellular electrophysiology of canine pulmonary vein cardiomyocytes: action potential and ionic current properties." *Journal of Physiology*, vol 551 pp. 801-813, 2003.

[5] E.M. Cherry, J.R. Ehrlich, S. Nattel, F.H. Fenton. "Pulmonary vein reentry - properties and size matter: insights from a computational analysis." *Heart Rhythm*, vol 4 pp. 1553-1562, 2007.

[6] DM. Harrild, C.S. Henriquez. "A computer model of normal conduction in the human atria." *Circulation Research*, vol 87, pp. 25-36, 2000.

[7] N. Virag, V. Jacquemet, C.S. Henriquez, S. Zozor, O. Blanc, J.M. Vesin, E. Pruvot, L. Kappenberger. "Study of atrial arrhythmias in a computer model based on MR images of human atria." *Chaos*, vol 12, pp. 754-763, 2002.

[8] G. Seemann, C. Höper, F.B. Sachse, O. Dössel, A.V. Holden, H.G. Zhang. "Heterogeneous three-dimensional anatomical and electrophysiological model of human atria." *Philosophical. Transactions of the Royal Society. Series A,* vol 364: pp. 1465-1481, 2005.

[9] O. Aslanidi, M. Boyett, J. Li, H. Dobrzynski, H. Zhang. "Mechanisms of transition from normal to reentrant electrical activity in a model of rabbit atrial tissue: interaction of tissue heterogeneity and anisotropy." *Biophysical Journal*, vol 96, pp. 798-817, 2009.

[10] O. Aslanidi, M.A. Colman, J Stott, H Dobrzynski, M. Boyett, A.V. Holden, H. Zhang. "3D virtual human atria: A computational platform for studying clinical atrial fibrillation." *Progress in Biophysics and Molecular Biology.,* vol 107, pp. 156-168, 2011.

[11] M.W. Krueger, V. Schmidt, C. Tobon, F.M. Weber, C. Lorenz, D.U.J. Keller, H. Barschdorf, M. Burdumy, P. Neher, G. Plank, K. Rhode, G. Seeman, D. Sánchez-Quintana, J. Saiz, R. Razavi, O. Dossel. "Modeling atrial fiber orientation in patient-specific geometries: a semi-automatic rule-based approach." in Functional Imaging and Modeling of the Heart 2011, Lecture Notes in Computer Science, L. Axel and D. Metaxis, Eds., vol 6666, pp. 223-232, 2011.

[12] M.W. Krueger, G. Seeman, K. Rhode, D.U.J. Keller, C. Schilling, A. Arunjuna, J. Gill, M.D. O'Neill, R. Razavi, O. Dossel. "Personalization of atrial anatomy and electrophysiology as a basis for clinical modeling of radio-frequency-ablation of atrial fibrillation." IEEE Transactions in Biomedical Imaging, vol 31, In press, 2012.

[13] J-C. Zhao, T.D. Butters, H Zhang, A.J. Pullan, I.J. Legrice, G.B. Sands, B.H. Smaill,. "An image-based model of atrial muscular architecture: Effects of structural anisotropy on electrical activation." *Circulation: Arrhythmia and Electrophysiology,* vol 5, pp. 361-370, 2012.

[14] K. Wang, S.Y. Ho, D.G. Gibson, R.H. Anderson. "Architecture of atrial musculature in humans." *Heart,* vol 73, pp. 559-565, 1995.

[15] S.Y. Ho, D. Sánchez-Quintana. "The importance of atrial structure and fibers." *Clinical Anatomy,* vol 2, pp. 52-63, 2009.

[16] D.A. Gerneke, G.B. Sands, R. Ganesalingam, P. Joshi, B.J. Caldwell, B.H. Smaill, I.J. Legrice. "Surface imaging microscopy using an ultramiller for large volume 3D reconstruction of wax- and resin-embedded tissues." *Microscopy Research and Technique,* vol 70, pp. 886-894, 2007.

[17] A. Frangi, W. Niessen, K. Vincken, M. Viergever. Multiscale Vessel Enhancement Filtering. *Lecture Notes in Computer Science.* pp. 130–137, 1998.

[18] B. Jähne. "Digital image processing." 6th ed. Springer-Verlag, The Netherlands, 2005.

[19] W.J. Karlon, J.W. Covell, A.D. McCulloch, J.J. Hunter, J.H. Omens. "Automated measurement of myofiber disarray in transgenic mice with ventricular expression of ras." *Anatomical Record*, vol 252, pp. 612-625, 1998.

[20] J-C. Zhao, M.L. Trew, I.J. Legrice, B.H. Smaill, A.J. Pullan. "A tissue-specific model of reentry in the right atrial appendage." *Journal of Cardiovascular Electrophysiology,* vol 20, pp. 675-684, 2009.

[21] M. Axelsson. Estimating 3D fiber orientation in volume images. *Proceedings of 19th International Conference on Pattern Recognition*. 2008.

[22] J. Weickert. "Anisotropic diffusion in image processing." Stuttgart, Germany: Teubner-Verlag. 1998.

[23] G.S. Watson. "Statistcs on spheres." Lecture notes in mathematical sciences 6 New York: John Wiley, 1983.

[24] M. Courtemanche, R.J. Ramirez, S. Nattel. "Ionic mechanisms underlying human atrial action potential properties: insights from a mathematical model." *American Journal of Physiology: Heart and Circulatory Physiology*, vol 275, pp. H301-H321, 1998.

[25] R.A. Gray, A.M. Pertsov, J. Jalife. "Incomplete reentry and epicardial breakthrough patterns during atrial fibrillation in the sheep heart." *Circulation,* vol 94, pp. 2649 –2661, 1996.

[26] F. Fenton, A. Karma. "Vortex dynamics in three-dimensional continuous myocardium with fiber rotation: Filament instability and fibrillation." *Chaos*, vol 8, pp. 20-47, 1998.

[27] R.A. Oliver, W. Krassowska. "Reproducing cardiac restitution properties using the Fenton-Karma membrane model." *Annals of Biomedical Engineering*, vol 33, pp. 907-911, 2005.

[28] A.M. Goodman, R.A. Oliver, C.S. Henriquez, P.D. Wolf. "A membrane model of electrically remodelled atrial myocardium derived from in vivo measurements." Europace, vol 7, S135-S145, 2005.

[29] M.S. Spach, W.T. Miller, D.B. Geselowitz, R.C. Barr, J.M. Kootsey, E.A. Johnson. "The discontinuous nature of propagation in normal canine cardiac muscle: evidence for recurrent discontinuities of intracellular resistance that affect the membrane currents." *Circlation Research,* vol 48, pp. 39-54, 1981.

[30] J.P. Boineau, R.B. Schuessler, C.R. Mooney, C.B. Miller, A.C. Wylds, R.D. Hudson, J.M. Borremans, C.W. Brockus. "Natural and evoked atrial flutter due to circus movement in dogs: Role of abnormal atrial pathways, slow conduction, refractory period distribution and premature beats." *American Journal of Cardioiology*, vol 45, pp. 1167–1181, 1980.

[31] P.C. Dolber, M.S. Spach. "Structure of Bachmann's bundle related to propagation of excitation." *American Journal of Physiology: Heart and Circulatory Physiology*, vol 257, pp. H1446–H1457, 1989.

[32] M.S. Spach, W.T. Miller III, P.C. Dolber, J.M. Kootsey, J.R. Sommer, C.E. Mosher Jr. "The functional role of structural complexities in the propagation of depolarization in the atrium of the dog: cardiac conduction disturbances due to discontinuities of effective axial resistivity." *Circulation Research,* vol 50, pp. 175–191, 1982.

[33] H. Hayashi, R. Lux, R. Wyatt, M.J. Burgess, J.A. Abildskov. "Relation of canine atrial activation sequence to anatomic landmarks." *American Journal of Physiology: Heart and Circulatory Physiology,* vol 242, pp. H421–H428, 1982.

[34] O. Berenfeld, A.V. Zaitsev. "The muscular network of the sheep right atrium and frequency-dependent breakdown of wave propagation." *Anatical Record,* vol 280A, pp. 1053–1061, 2004.

[35] A. Hansson, M. Holm, P. Blomstrom, R. Johansson, C. Luhrs, J. Brandt, S. Olsson. "Right atrial free wall conduction velocity and degree of anisotropy in patients with stable sinus rhythm studied during open heart surgery." *European Heart J*ournal, vol 19, pp. 293–300, 1998.

[36] S. Mori, P. Zijl. "Fiber tracking: principles and strategies – a technical review." *NMR in Biomedicine*, vol 15, pp. 468-480, 2002.

[37] S. Verheule, E.E. Wilson, R. Arora, S.K. Engle, L.R. Scott, J.E. Olgin. "Tissue structure and connexin expression of canine pulmonary veins." *Cardiovascular Research*, vol 55, pp. 727-738, 2002.

[38] R.J. Hassink, H.T. Aretz, J. Ruskin, D. Keane. "Morphology of atrial myocardium in human pulmonary veins: a postmortem analysis in patients with and without atrial fibrillation." *Journal of the American College of Cardiology,* vol 42, pp. 1108-1114, 2003.

[39] R.S. Stephenson, M.R. Boyett, G. Hart, T. Nikolaidou, X. Cai, A. F. Corno, N. Alphonso, N. Jeffery, J.C. Jarvis. "Contrast enhanced micro-computed tomography resolves the 3-dimensional morphology of the cardiac conduction system in mammalian hearts." *PloS one*, vol. 7(4), 2012.

[40] O. Aslanidi, T. ikolaidou, J. Zhao, B. Smaill, S. Gilbert, J. Jarvis, R. Stephenson, J. Hancox, M. Boyett, H. Zhang. "Application of micro-computed tomography with iodine staining to cardiac imaging, segmentation and computational model development." *IEEE Transactions in Biomedical Imaging*, vol 31, In press, 2012.

[41] R. De Ponti, S.Y. Ho, J.A. Salerno-Uriarte, M. Tritto, G. Spadacini. "Electroanatomic analysis of sinus impulse propagation in normal human atria." *Journal of Cardiovascular Electrophysiology,* vol 13, pp. 1-10, 2002.

[42] S.-I. Sakamoto, T. Nitta, Y. Ishii, Y. Miyagi, H. Ohmori, K. Shimizu. "Interatrial electrical connections: the precise location and preferential conduction." *Journal of Cardiovascular Electrophysiology,* vol 16, pp. 1077-1086, 2005.

[43] W.M. Hartung, D. Hartung, H. Saad, A. Mittag, D. Mahnkopf, H.U. Klein, R. Willems. "The importance of right atrial pacing configuration for intra-atrial and inter-atrial conduction times." *Journal of Interventional Cardiac Electrophysiology,* vol 4, pp. 405-413, 2000.

[44] M. Yamazaki, S. Mironov, C. Taravant, J. Brec, L.M. Vaquero, K. Bandaru, U.M.R. Avula, H. Honjo, I. Kodama, O. Berenfeld, J. Kalifa. "Heterogeneous atrial wall thickness and stretch promote scroll waves anchoring during atrial fibrillation." *Cardiovascular Research*, vol 94, pp. 48-57, 2012.

[45] V. Jacquemet. "An eikonal-diffusion solver and its application to the interpolation and the simulation of reentrant cardiac activations." C*omputer Methods and Programs in Biomedicine,* (doi:10.1016/j.cmpb.2111.05.2003), 2011.

[46] M Sermesant, E Konukoglu, H Delingette, Y Coudiere, P Chinchapatnam, KS Rhode, R Razavi, N Ayache. "An anisotropic multi-front fast marching method for real-time simulation of cardiac electrophysiology." *FIMH* edited by FB Sachse and G Seemann, LNCS 4466, pp. 160-169, 2007.

[47] J Relan, M Sermesant, H Delingette, N Ayache. "Personalisation of a 3D ventricular electrophysiological model, using endocardial and epicardial contact mapping and MRI." *STACOM* edited by Camara et al., LNCS 7085, pp. 14-22, 2012.